AIAA JOURNAL
Vol. 37, No. 2, February 1999

Calculation of Basic Sound Radiation of Axisymmetric Jets by Direct Numerical Simulations

E. J. Avital,* N. D. Sandham,† and K. H. Luo‡
Queen Mary and Westfield College, London, England E1 4NS, United Kingdom
and
R. E. Musafir§
Universidade Federal do Rio de Janeiro, 21945 Rio de Janeiro, Brazil

The basic radiation of sound from forced laminar axisymmetric jets ($Re_D = 6 \times 10^2$ to 1.5×10^3) is calculated by a hybrid approach, whereby the hydrodynamic field is calculated by an incompressible stream function–vorticity direct numerical simulation (DNS) and the sound field is calculated by the compact Lighthill and Möhring–Kambe formulations. It is shown that, because of the oscillatory behavior of the source as a wave packet, the acoustic results are more sensitive to numerical constraints such as the DNS box size than are the hydrodynamic results. Lighthill's formulation shows a strong sensitivity to the radial boundary condition imposed on the velocity in the DNS. A zero second-order radial derivative for the stream function behaves the best, and a zero radial velocity condition behaves the worst. The Möhring–Kambe formulation shows a strong dependence on the arbitrary location of the coordinate origin. A boundary correction developed to eliminate this dependence is shown to work well by achieving a good agreement between the two formulations in the dominant features of the sound radiation. The effects of the inflow momentum thickness and Reynolds number are investigated with reference to the directivity and frequency spectrum of the emitted sound.

I. Introduction

THIS work concentrates on the sound generated by the mixing region of a low subsonic circular jet. This region has a vital role in the sound production,[1] and experimentally it was found that the region is dominated by large-scale structures when the jet is forced by a coherent disturbance.[2] These large structures have the appearance of instability waves, initially growing, then saturating and decaying.[1] Thus, they can be referred to as wave packets and have been found to be responsible for the appearance of strong discrete peaks in the frequency spectrum of the far-field sound.[3] Wave packets models have also been used to explain the appearance of superdirective sound field,[4] to investigate the structure of the sound field,[5] and to estimate the axial length of a computational box required for a direct simulation of such a sound field.[6]

The only computational study that includes simulating the mixing region by the direct numerical simulation (DNS) method has been carried by Mitchell et al.[7] The DNS method solves the full Navier–Stokes equations without any modeling. The Mitchell et al.[7] approach was a spatial one, meaning that inflow and outflow boundary conditions are specified and any artificial coupling between them is eliminated or at least minimized. This results in the jet evolving by a spatial instability mechanism. The sound generation was calculated directly by a compressible DNS for an axisymmetric jet and compared to indirect calculations using Lighthill's acoustic analogy and the Kirchoff surface method, with a reasonable agreement for the former and a better agreement for the latter. The calculations were carried for various Mach numbers, but only for one specific configuration of an inflow condition, a Reynolds number, and a computational box size. One of the aims of the current work is to expand the experience in using DNS for aeroacoustic calculations of circular jet noise.

An important aspect of subsonic jet noise is its low Mach number jet range as argued by Crighton.[8] This range is dominated by the so-called basic radiation pattern, and many aspects of high-velocity effects such as convection and refraction can be represented as multiplicative corrections to that radiation.[8] The appropriate approach for calculating basic radiation is the hybrid method, where only the source/hydrodynamic field is simulated and the sound is calculated by an aeroacoustic method.[9] This method has two computational advantages for basic radiation. The first is that the hydrodynamic field can be considered as incompressible.[9] This reduces the computational resources required for the DNS by having fewer properties to solve and a higher stability limit on the time step due to the exclusion of the sound field. The second advantage is that the sound itself can be calculated by a compact approximation of a Green's function solution of an acoustic analogy, i.e., assuming the sound wavelength is much longer than the source length scale. This allows the omission of the retarded time variation along the source, which leads to a reduction in the computational resources and a simplification in the computational procedure. Extensions to include the retarded time variation are possible[10] and will be discussed in the future. In this study, we concentrate on getting the basic radiation source correctly, which is an essential step, before considering the retarded time variation.

The result that basic radiation source is compact means the source has a finite size. This eliminates the option of the relatively inexpensive temporal DNS approach for this kind of calculation, at least for the large-scale source. This is because the temporal approach uses periodic axial boundary conditions, i.e., the jet evolves by a temporal instability process. This results in an infinite axial length for the large-scale source.[11] It leaves us with the more expensive option of spatial DNS. However, even with spatial DNS much care is needed to set up the problem. As an example, the finite computational box can cut the source and cause distortion in the sound calculation.[6] A correction for Lighthill's formulation was suggested to reduce that effect.[10] Nevertheless, this emphasizes the importance of checking the effect of numerical parameters, such as the box size and boundary conditions on the calculation accuracy, before contemplating a full three-dimensional simulation.

The axisymmetric case allows a unique situation of an inexpensive two-dimensional simulation of a three-dimensional finite

Received April 10, 1998; presented as Paper 98-2263 at the AIAA 19th Aeroacoustics Conference, Toulouse, France, June 2–4, 1998; revision received Oct. 10, 1998; accepted for publication Oct. 13, 1998.

*Postdoctoral Research Assistant, Department of Engineering, Mile End Road. Member AIAA.
†Reader, Department of Engineering, Mile End Road. Member AIAA.
‡Senior Lecturer, Department of Engineering, Mile End Road. Member AIAA.
§Associate Professor, Mechanical Engineering and Hydraulics Department, C.P. 68503.

source. This allows a comparison of different compact solutions that were developed for such sources. However, the axisymmetric constraint does limit the range of the phenomena because lateral quadrupoles become zero in the compact limit and a transition to fine scale turbulence is prevented. Nevertheless, the success of models[12] that assume dominance of the longitudinal quadrupoles, in which the axisymmetric mode has a significant role and the characteristics of axisymmetric emission found in experiments,[13] points to the importance of this mode in the sound field emitted by large-scale sources. Thus, any simulation trying to predict a large-scale sound field must be able to capture the axisymmetric component correctly.

The objectives of the study are 1) to test the effects of various numerical parameters on the basic radiation calculation for the axisymmetric mode, 2) to improve the prediction of the acoustic analogies solution for that case, and 3) to study the structure of the axisymmetric source of basic radiation for different inflow configurations and Reynolds numbers. The hydrodynamic formulation for the incompressible DNS is presented in Sec. II. The acoustic analogy formulation is discussed in Sec. III, and the results are discussed in Sec. IV.

II. Hydrodynamic Formulation

One of the most efficient formulations for incompressible two-dimensional DNS is the stream function–vorticity (ψ–ω) formulation. It automatically satisfies continuity and reduces the number of solved properties from three (p, u, v) to two (ψ, ω). The analytical formulation for the axisymmetric jet is presented in Sec. II.A, and the numerical method is discussed in Sec. II.B.

A. Analytic Formulation

The conservative form of the vorticity equation of an axisymmetric flow is

$$\frac{\partial \omega_\phi}{\partial t}+\frac{\partial (v_r \omega_\phi)}{\partial r}+\frac{\partial (v_x \omega_\phi)}{\partial x}=\frac{1}{Re_D}\left\{\frac{\partial}{\partial r}\left[\frac{1}{r}\frac{\partial (r\omega_\phi)}{\partial r}\right]+\frac{\partial^2 \omega_\phi}{\partial x^2}\right\} \tag{1}$$

where $Re_D \equiv \rho U_J D/\mu$ with U_J the inflow jet mean velocity at the centerline and D the inflow jet diameter. The velocities v_r and v_x are normalized by U_J, vorticity ω_ϕ by U_J/D, distances r and x by D, and time t by D/U_J. The formulation can be closed by the kinematics relations

$$v_r=-\frac{1}{r}\frac{\partial \psi}{\partial x}, \qquad v_x=\frac{1}{r}\frac{\partial \psi}{\partial r} \tag{2}$$

$$-\omega_\phi=\frac{\partial}{\partial r}\left(\frac{1}{r}\frac{\partial \psi}{\partial r}\right)+\frac{1}{r}\frac{\partial^2 \psi}{\partial x^2} \tag{3}$$

An additional property of a passive scalar $f_{\rm ps}$ governed by

$$\frac{\partial f_{\rm ps}}{\partial t}+\frac{1}{r}\frac{\partial (r v_r f_{\rm ps})}{\partial r}+\frac{\partial (v_x f_{\rm ps})}{\partial x}=\frac{1}{Re_D Sc}\left[\frac{1}{r}\frac{\partial}{\partial r}\left(r\frac{\partial f_{\rm ps}}{\partial r}\right)+\frac{\partial^2 f_{\rm ps}}{\partial x^2}\right] \tag{4}$$

where $Sc=1$, was also simulated to provide an illustration tool for the flow, to compute mixing characteristics, and to provide an indicator to the hydrodynamic resolution.[14]

Inflow Dirichlet boundary condition are prescribed for the velocities[15]

$$v_r(r, x=0)=0, \qquad v_x(r, x=0)=U(r)\left(1+\sum_{i=1}^{N} a_i \sin \omega_i t\right) \tag{5}$$

where $U(r)$ is an appropriate profile describing a laminar jet starting its mixing stage and $\sum a_i \sin \omega_i t$ is the disturbance. The mean inflow axial velocity is taken as[16]

$$U(r)=0.5\{1+\tanh[b_2(R/r-r/R)]\}, \qquad b_2=0.25R/\delta_2 \tag{6}$$

where R is the inflow radius defined as the point where the mean streamwise velocity is half of its centerline value and δ_2 is the momentum thickness defined as

$$\delta_2 \equiv \int_0^\infty \frac{U(r)}{U(r=0)}\left[1-\frac{U(r)}{U(r=0)}\right]{\rm d}r \tag{7}$$

Soft boundary conditions of the form

$$\frac{\partial f}{\partial t}+U_c\frac{\partial f}{\partial x}=0, \qquad x=L_x \tag{8}$$

are prescribed at the outflow for the vorticity and the streamwise velocity, i.e., these properties are assumed to leave as frozen structures. It is common to take U_c as a constant representing an average convective velocity.[17] The typical eddy convection velocity is quoted by Lighthill[18] as 0.5–0.6 times the jet exit speed. In this study U_c of Eq. (8) is taken as half of the instantaneous centerline velocity. Changing this ratio to 0.7 (the U_c of simulated flow structures) or taking U_c as the instantaneous local axial velocity proved to have negligible effect on the hydrodynamic results and on the acoustic results as long as the aeroacoustic calculations were kept an axial length of about $4D$ away from the outflow. Wang et al.[9] suggested improving Eq. (8) for DNS of boundary layers on a flat plate by taking U_c as one and adding $\partial f_{\rm mean}/\partial x$ to the right-hand side of Eq. (8). The value $f_{\rm mean}$ was calculated by laminar boundary-layer theory for steady flow. Implementing this modification to the current case proved to have the same small effect as changing U_c of Eq. (8) from 50 to 70% of the instantaneous centerline velocity

The boundary conditions at the centerline are taken as

$$\omega_\phi(r=0, x)=0, \qquad v_r(r=0, x)=0 \Rightarrow \psi(r=0, x)=\text{const} \tag{9}$$

due to the axisymmetry. The vorticity is also expected to decay rapidly outside the jet, and so at the outer edge of the box it is assumed that

$$\omega_\phi(r=L_r, x)=0 \tag{10}$$

Three types of boundary conditions required for the velocity field at the radial edge of the box are to be tested. The first is a no-penetration condition

$$v_r|_{r=L_r}=0 \Rightarrow \psi_{r=L_r}=\text{const} \tag{11}$$

where the constant is set by integrating $v_x(r, x=0)$ along the radial direction. The second type is a free slip condition

$$\left.\frac{\partial v_x}{\partial r}\right|_{r=L_r}=0 \tag{12}$$

Analytically, Eqs. (11) and (12) are identical because of Eq. (10) and the zero-inflow radial velocity (5). However, it is shown in Sec. IV that these two conditions can have a different numerical effect on the acoustic results. The third type of boundary condition is

$$\left.\frac{\partial^2 \psi}{\partial r^2}\right|_{r=L_r}=0 \tag{13}$$

It is common to assume a parallel flow as the initial condition at $t=0$, because it automatically satisfies continuity. Here it is taken as $v_r=0$, $v_x=U(r)$. Consequently, the initial conditions for ω_ϕ and ψ are set by Eqs. (2) and (3). The initial condition for the passive scalar is as for the vorticity, but normalized by the maximum value, to provide an initial range between zero and one. This distribution also serves as the inflow condition for the passive scalar, while the rest of the boundary conditions are as for ω_ϕ.

B. Numerical Method

A second-order central finite difference scheme is used for the spatial discretization of Eqs. (1–3). A second-order backward scheme is used to implement the outflow boundary condition (8). The inflow boundary condition for ω_ϕ is determined by Eqs. (3) and (5) and a second-order-accurate one-sided formula[19] for $\partial^2\psi/\partial x^2$ at $x=0$. Changing that formula to a first order-accurate one proved to have a negligible effect on the results.

The centerline velocity, which is needed for estimating U_c in Eq. (8), can be calculated by

$$U_{\rm cl}=\frac{1}{2}\left.\frac{\partial^2 \psi}{\partial r^2}\right|_{r=0} \tag{14}$$

due to axisymmetry, and a second order-accurate one-sided formula. The elliptic equation (3) is solved by a fast solver that uses a fast sine-Fourier transform in the axial direction and a tridiagonal solver in the radial direction. Numerical stability analysis of Eq. (1) shows that the convection part is much more crucial in setting the limit on the time-marching step than the diffusion part for the cases studied in Sec. IV. Thus, the vorticity equation (1) is marched explicitly in time by a third-order compact Runge–Kutta scheme, saving by that the need for an additional elliptic solver required by an implicit marching of the diffusion part. The DNS code was checked by a comparison to analytical solutions of a Stokes problem and to results produced by a steady-state laminar boundary-layer code.

III. Aeroacoustic Formulation

Basic radiation solutions are based on compact quadrupole source expressions valid for $M \to 0$. Two formulations of basic radiation are investigated in this study. The first is Lighthill's formulation[8] that uses the velocity field to express the source. The second is Möhring–Kambe's formulation[20] that mainly uses the vorticity field for that purpose and, thus, is convenient for the present (ψ–ω) DNS. Both formulations are based on the linear wave operator for a stationary medium and, thus, should yield the same results if the assumptions they are based on are met.

A. Lighthill's Formulation

For an axisymmetric flow, i.e., with no azimuthal variation in any flow quantities, the lateral quadrupoles are zero in the compact limit. Thus, the total acoustic power output P and the directivity $D(\theta)$ can be defined as

$$P = \frac{\rho_0}{8\pi c_0^5}\int_0^\pi D(\theta)\sin\theta\,\mathrm{d}\theta \tag{15a}$$

$$D(\theta) = \overline{\left(\ddot{Q}_{11}\cos^2\theta + \ddot{Q}_{22}\sin^2\theta\right)^2} \tag{15b}$$

$$\ddot{Q}_{11} = 2\pi\frac{\partial^2}{\partial t^2}\int\!\!\int v_x^2 r\,\mathrm{d}r\,\mathrm{d}x, \qquad \ddot{Q}_{22} = \pi\frac{\partial^2}{\partial t^2}\int\!\!\int v_r^2 r\,\mathrm{d}r\,\mathrm{d}x \tag{15c}$$

where θ is the downstream angle, $\ddot{Q}_{11}$ and $\ddot{Q}_{22}$ are the longitudinal quadrupoles, ρ_0 is the ambient density, and c_0 is the ambient speed of sound. Both ρ_0 and c_0 are taken as one. The overbar in Eq. (15b) denotes averaging in time and only the dominant contribution, which is of the instantaneous Reynolds stress,[9] is accounted in Eq. (15c). The integration in Eq. (15c) is performed over the entire source field. The overall frequency spectrum can be calculated by a Fourier transform of $\ddot{Q}_{11}$ and $\ddot{Q}_{22}$.

The jet is considered as a point source in Eq. (15). However, it is important to identify the contributions of different parts of the jet to the integration in Eq. (15c), especially in the axial direction. Following Lighthill,[21] an acoustic power output distribution $P(x)$ is defined as

$$P(x) = \alpha_{ij}\ddot{Q}_{ii}\int^x \ddot{q}_{jj}\,\mathrm{d}\xi \tag{16a}$$

where

$$\ddot{q}_{11} = 2\pi\frac{\partial^2}{\partial t^2}\int v_x^2 r\,\mathrm{d}r, \qquad \ddot{q}_{22} = \pi\frac{\partial^2}{\partial t^2}\int v_r^2 r\,\mathrm{d}r \tag{16b}$$

and α_{ij} can be found from Eq. (15) after performing the integration with respect to θ. The acoustic power output per axial length can be found by differentiating Eq. (16a) with respect to x, which leads after evaluating α_{ij} to

$$\frac{\mathrm{d}P(x)}{\mathrm{d}x} = \frac{\rho_0}{20\pi c_0^5}\left[\overline{\ddot{Q}_{11}\ddot{q}_{11}} + 8\overline{\ddot{Q}_{22}\ddot{q}_{22}}/3 + 2\overline{(\ddot{Q}_{11}\ddot{q}_{22} + \ddot{Q}_{22}\ddot{q}_{11})}/3\right] \tag{17}$$

The compact source derivation that yields Eq. (15) is based on the assumption that the entire source field is contained in the integration limits. However, in practice the DNS box is finite, and the source is rarely entirely contained within it, especially in the axial direction, so that unphysical results may occur. For example, a frozen convecting structure should not emit basic radiation[1] and solution (15) upholds this property if the entire source is within the integration limits of Eq. (15c). However, what happens if that structure starts leaving the box? The integration interprets this as a diminishing structure, and as a result some spurious sound is calculated. Wang et al.[10] recognized this problem and suggested the addition of boundary corrections to the quadrupole calculation, leading to the general expression

$$\ddot{Q}_{ij} = \int_V \frac{\partial^2 T_{ij}}{\partial t^2}\,\mathrm{d}V + \int_S \frac{\partial T_{ij}}{\partial t}\boldsymbol{U}_c\cdot\mathrm{d}\boldsymbol{s} \tag{18}$$

where V is the DNS box, S is its surface, and $\boldsymbol{U}_c$ is the convective velocity of the large-scale structures leaving the box. The surface integral in Eq. (18) was shown to reduce the effect of the box size using a Taylor expansion.[10] Actually, this is the same as assuming a frozen convecting structure outside the box and, thus, is based on a similar assumption as the hydrodynamic outflow condition (8).

The effectiveness of the boundary correction in Eq. (18) can be demonstrated by a wave packet model. Huerre and Crighton[22] argued that the basic sound production is dominated by the axial longitudinal quadrupole, which in turn is dominated by the shear noise term. This makes $\ddot{q}_{11}$ proportional to $U_x\ddot{u}_x$, where U_x is the mean streamwise velocity and u_x is the perturbation velocity in that direction. Neglecting the weak axial variation in U_x and assuming u_x varies as a wave packet in the axial direction leads to

$$\ddot{q}_{11} = A(\varepsilon x)e^{ix-it}, \qquad \varepsilon \ll 1, \qquad -L_x/2 \le x \le L_x/2 \tag{19}$$

where for simplicity the wave number and the frequency in the exponent are taken as one, making $U_c = 1$. A is the packet envelope, and its maximum is assumed to be at the box center. P is proportional to $\ddot{Q}_{11}^2$ by Eq. (15), and an integration by parts shows that the correction in Eq. (18) reduces the error in P from

$$\frac{|\Delta P|}{P(L_x\to\infty)} = \frac{2\varepsilon A(\varepsilon L_x/2)}{\pi\hat{A}(-1/\varepsilon)} + \mathcal{O}(\varepsilon^2) \tag{20a}$$

where $\hat{A}$ is the Fourier transform of $A(X)$, to

$$\frac{|\Delta P|}{P(L_x\to\infty)} = \frac{2\varepsilon^2|A'(\varepsilon L_x/2)|}{\pi\hat{A}(-1/\varepsilon)} + \mathcal{O}(\varepsilon^3) \tag{20b}$$

where $\Delta P \equiv P(L_x) - P(L_x\to\infty)$, and it is assumed

$$|\Delta P|/P(L_x\to\infty) < \mathcal{O}(1)$$

Thus, Eq. (18) has the same effect as the wave packet was continuing with a constant amplitude outside of the box. This effect is shown in Fig. 1 for the exponential wave packet envelope suggested by Crighton and Huerre.[4] Other forms of packets such as algebraic and Gaussian[4] also showed improvement when Eq. (18) was implemented.

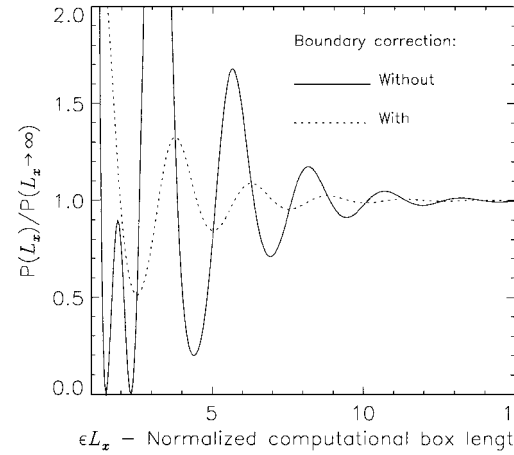

Fig. 1 Variation of the acoustic power output with the computational box length L_x for Lighthill's source modeled as an exponential wave packet with $\varepsilon = 0.2$, showing the effect of the boundary correction given by Eq. (18).

B. Möhring–Kambe's Formulation

The main achievement of Möhring was to express the basic radiation source by the vorticity only for an inviscid fluid.[8] This formulation was later extended by Kambe[20] for a viscous fluid. Taking into account only the contribution from the Reynolds stress as in Sec. III.A, the total acoustic power output P and the directivity $D_M(\theta)$ can be defined as

$$P = \frac{\rho_0}{8\pi c_0^5}\int_0^{\pi} D_M(\theta)\sin\theta\,\mathrm{d}\theta \tag{21a}$$

$$D_M(\theta) = \overline{\left[\left(\cos^2\theta - \tfrac{1}{3}\right)\ddot{Q}_M + \tfrac{2}{3}\ddot{K}_M\right]^2} \tag{21b}$$

$$\ddot{Q}_M \equiv \pi\frac{\partial^3}{\partial t^3}\int\!\!\int (x - x_a)\omega_\phi r^2\,\mathrm{d}r\,\mathrm{d}x \tag{21c}$$

$$\ddot{K}_M \equiv \pi\frac{\partial^2}{\partial t^2}\int\!\!\int \left(v_x^2 + v_r^2\right) r\,\mathrm{d}r\,\mathrm{d}x \tag{21d}$$

where x_a is the axial location of the origin of the coordinate system. $\ddot{K}_M$ is the contribution from the fluctuations in the total kinetic energy and is zero for the inviscid case. In this case one gets a specific pattern with two minima at $\theta \cong 55$ and 125 deg for $D_M(\theta)$. That pattern can be recovered from Lighthill's formulation (15) by assuming constant total kinetic energy, giving $\ddot{Q}_{22} = -0.5\ddot{Q}_{11}$ due to axisymmetry.

It is important to note that unless

$$\frac{\partial^3}{\partial t^3}\int\!\!\int \omega_\phi r^2\,\mathrm{d}r\,\mathrm{d}x = 0 \tag{22}$$

$\ddot{Q}_M$ depends on the location of the coordinate origin x_a. It can be shown that Eq. (22) is fulfilled when the computational box contains the entire source field by the vorticity equation (1) and the divergence theorem. However, Eq. (22) does not necessarily hold for a finite box, which leads to an unphysical behavior of a dependence on the arbitrary location of the coordinate origin. This problem can be corrected by adding boundary corrections to $\ddot{Q}_M$. Assuming a frozen convecting structure outside of the box for ω_ϕ, one gets

$$\begin{aligned}\ddot{Q}_M = {} & \pi\int_0^{L_x}(x - x_a)\,\mathrm{d}x\int_0^{L_r}\frac{\partial^3\omega_\phi}{\partial t^3}r^2\,\mathrm{d}r \\ & + \pi\int_0^{L_r}\left[(x - x_a)U_c\frac{\partial^2\omega_\phi}{\partial t^2}\right]_{x=L_x} r^2\,\mathrm{d}r \\ & - \pi\int_0^{L_r}\left[(x - x_a)U_c\frac{\partial^2\omega_\phi}{\partial t^2}\right]_{x=0} r^2\,\mathrm{d}r \\ & + \pi\int_0^{L_r}\left[U_c^2\frac{\partial\omega_\phi}{\partial t}\right]_{x=L_x} r^2\,\mathrm{d}r \\ & - \pi\int_0^{L_r}\left[U_c^2\frac{\partial\omega_\phi}{\partial t}\right]_{x=0} r^2\,\mathrm{d}r\end{aligned} \tag{23}$$

where $\ddot{K}_M$ can be corrected by Eq. (18). However, Eq. (23) does not guarantee elimination of the dependence on x_a. Calculations using the wave packet model showed that it reduced that dependence but did not eliminate it.

To develop a boundary correction that analytically eliminates the dependence on x_a, we begin with a generalized version of Eq. (23)

$$\begin{aligned}\ddot{Q}_M = {} & \pi\int_0^{L_x}(x - x_a)\,\mathrm{d}x\int_0^{L_r}\frac{\partial^3\omega_\phi}{\partial t^3}r^2\,\mathrm{d}r \\ & + \pi\int_0^{L_r}\left[(x - x_a)f_M\right]_{x=L_x}\mathrm{d}r - \pi\int_0^{L_r}\left[(x - x_a)f_M\right]_{x=0}\mathrm{d}r \\ & + \pi\int_0^{L_r} g_M|_{x=L_x}\,\mathrm{d}r - \pi\int_0^{L_r} g_M|_{x=0}\,\mathrm{d}r\end{aligned} \tag{24}$$

where f_M and g_M are unknowns. The form of f_M can be found by requiring Eq. (24) to be independent on x_a, meaning

$$\int_0^{L_x}\mathrm{d}x\int_0^{L_r}\frac{\partial^3\omega_\phi}{\partial t^3}r^2\,\mathrm{d}r + \int_0^{L_r} f_M|_{x=L_x}\,\mathrm{d}r - \int_0^{L_r} f_M|_{x=0}\,\mathrm{d}r = 0 \tag{25}$$

If the box is large enough to contain the entire source in the radial direction, then Eq. (1) can be used to show that

$$\int_0^{L_r}\frac{\partial^3\omega_\phi}{\partial t^3}r^2\,\mathrm{d}r = \frac{\partial F}{\partial x} \tag{26}$$

leading by Eq. (25) to

$$f_M = -\frac{\partial^2 v_r^2}{\partial t^2}r + \frac{\partial^2 v_x^2}{\partial t^2}r + \frac{\partial^2(v_x\omega_\phi)}{\partial t^2}r^2 - \frac{1}{Re_D}\frac{\partial^3\omega_\phi}{\partial x\,\partial t^2}r^2 \tag{27}$$

The similarity between Eqs. (23) and (27) is in the term $v_x\omega_\phi$, which partly explains the ability of Eq. (23) to reduce the dependence on x_a. The function g_M is left undefined. One option is to take $g_M = 0$; another is

$$g_M = U_c^2\frac{\partial\omega_\phi}{\partial t}r^2 \tag{28}$$

on the grounds of the similarity between Eqs. (23) and (27). Both options are checked in Sec. IV.

The numerical operations required for the aeroacoustic calculations were done by a trapezoidal role for spatial integrations and a second-order central difference scheme for the time differentiation. The third-order time derivative in Eq. (24) was evaluated as a second-order derivative using Eq. (1), thus reducing the computational resolution needed for the success of the boundary correction in Eq. (24).

IV. Results

The inflow was perturbed by a single frequency disturbance, as by Grinstein and Devore.[15] The frequency was set to $St_D = 0.3$ as in the experiments of Crow and Champagne.[2] This frequency corresponds to the jet preferred mode, where the disturbance is highly amplified.[1] The forcing amplitude was set to 2% of the inflow mean axial velocity, as by Crow and Champagne.[2] Most of the simulations were performed for the inflow momentum thickness set by $R/\delta_2 = 10$. This ratio is somewhat low but still fits into the practical range discussed by Michalke.[16] The Reynolds numbers were taken as $Re_D = 6\times10^2$ and 1.5×10^3.

The spatial resolution for $Re_D = 6\times10^2$ was set to (20, 20) points for a segment of $(x = D, r = R)$ and (30, 30) points for $Re_D = 1.5\times10^3$. The time-marching step was taken as half of the upper limit given by a numerical instability analysis based on a periodic boundary condition assumption.[14] The resolution was checked by monitoring the passive scalar evolution and by refining the mesh with 50% more points in each direction. The boundary correction (24) required a higher resolution of (40, 40) points at $Re_D = 1.5\times10^3$ to eliminate totally the dependence on x_a. The flow was allowed to evolve to a periodic limit cycle stage before the aeroacoustic statistics were accumulated. Because the main topic of the investigation is the aeroacoustic calculations, the hydrodynamic results are only briefly discussed in Sec. IV.A. The aeroacoustic results are discussed in Sec. IV.B.

A. Hydrodynamic Results

The simulations showed that a radial length of $6R$ was sufficient to make the effect of the radial length of DNS box L_r negligible for the results shown in Figs. 2 and 3, for any of the radial boundary conditions considered in Sec. II. The effect of the outflow boundary condition (8) was found to be confined to an axial length of about $1D$ before the outflow. Figure 2 shows the downstream evolution of the mean centerline velocity and the rms of that velocity. It shows that decreasing Re_D or increasing δ_2 has a damping effect on the perturbation growth, as can be expected from a Kelvin–Helmholtz instability process. It also shows that, at $Re_D = 1.5\times10^3$, δ_2 has a damping effect on the mean centerline velocity near the inflow. This kind of a minimum in the mean centerline velocity near the inflow was also found experimentally in turbulent jets.[2] As in that case, it is

caused by a nonlinear effect of the perturbation as shown by the high level of the rms maximum at $Re_D = 1.5 \times 10^3$. The rms maximum level for $Re_D = 1.5 \times 10^3$ and its location at $x \approx 5D$ correspond to the order reported in the turbulent jets experiments.[2] This correspondence is in line with the linear instability prediction in Michalke[16] of a small effect of Re_D for $Re_D > 1 \times 10^3$ and this type of inflow velocity profile. However, unlike the turbulent jets experiments, the rms plots do not show a second peak distribution due to the lack of background noise and natural turbulence. An example of the vorticity evolution is shown in Fig. 3 for $Re_D = 1.5 \times 10^3$, $R/\delta_2 = 10$. It shows a sequence of decaying vortex rings. This sequence will be shown to be responsible for the appearance of the sound source as the wave packet form discussed in Sec. III.A.

B. Aeroacoustic Results

Figure 4 shows the downstream evolution of the rms of Lighthill's quadrupoles per unit length calculated from Eq. (16b) for the three types of radial boundary conditions considered in Sec. II, with $Re_D = 6 \times 10^2$ and $R/\delta_2 = 10$. All profiles have a single maximum at about the same location where the rms of the centerline velocity has its maximum. The effect of the boundary condition becomes noticeable only when the rms of $\ddot{q}_{11}$ declines to less than 1% of its maximum and the rms of $\ddot{q}_{22}$ falls to less than 0.05% of its maximum. Only the profiles computed with boundary condition (13) continue to decline smoothly afterward. The other profiles exhibit fluctuations, a strong increase near the outflow for $\ddot{q}_{22}$, and a level-off for $\ddot{q}_{11}$, when boundary condition (11) is used. This is a pure numerical behavior that was found to decay as the radial length of the box L_r was increased.

The effects of the different radial boundary conditions on the directivity are shown in Fig. 5, where l_x in the figure caption is defined as the axial length stretching from $x = 0$ of the segment that is taken into account in the acoustic solution (15). U_c of the acoustic boundary correction (18) was taken as half of the instantaneous centerline velocity in this case. Figure 5 shows that the radial emission, i.e., $\theta \approx 90$ deg, is much less affected by an increase in l_x than the axial emission, i.e., $\theta \approx 0$ and 180 deg, which is due to the faster decline of the rms of $\ddot{q}_{22}$, as shown by Fig. 4. The convergence in the axial emission as l_x is increased is best when boundary condition (13) is used and worst when boundary condition (11) is used. In the case of boundary condition (11), there is a difference of about 8 dB in the axial emission between $l_x = 15D$ and $l_x = 35D$. Furthermore, there is about 4-dB difference in the axial emission between boundary conditions (11) and (13) for $l_x = 15D$. This shows that even the small fluctuations caused by the use of boundary condition (11) at $x < 15D$, and shown in Fig. 4a, have a significant effect on the accuracy of the acoustic results.

The reason for the extreme sensitivity of the acoustic results to small changes in the rms of $\ddot{q}_{11}$ is revealed in Fig. 6. It shows the downstream evolution of $\mathrm{d}P(x)/\mathrm{d}x$ as defined by Eq. (17). It reveals a wave packet structure as predicted in Sec. III. On a linear scale, the amplitude variation is smooth for all of the profiles, and the cause for the difference in the amplitude magnitude between the different profiles is not revealed. However, on a logarithmic scale, the smooth decay is lost at $x > 15D$ for the packets, which resulted from the use of boundary conditions (11) and (12). Section III showed that the DNS box has to capture the decaying tails of the wave packet for an accurate estimate of the acoustic power P. For a 5% error in P, it means capturing the packet down to 1% of its maximum amplitude for the exponential form of Sec. III and 0.01% for a similar Gaussian form. The effects of boundary conditions (11) and (12) are clearly in that range, and furthermore, the nonoscillatory behavior due to boundary condition (11) at $x > 20D$ makes things even worse.

The poor performance of the boundary conditions (11) and (12) can be explained as follows. Setting the radial velocity zero according to boundary condition (11) means a Dirichlet condition for

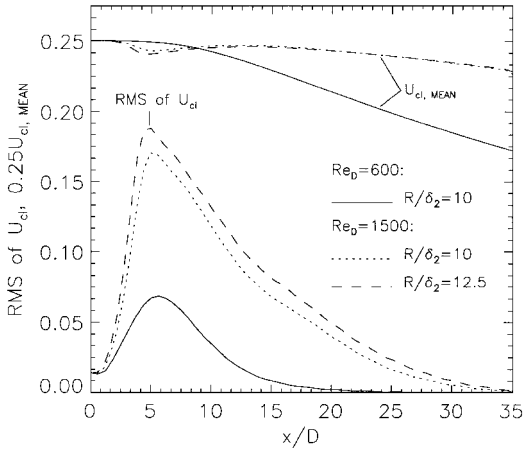

Fig. 2 Effects of the Reynolds number and the inflow momentum thickness δ_2 on the mean and rms of the centerline velocity.

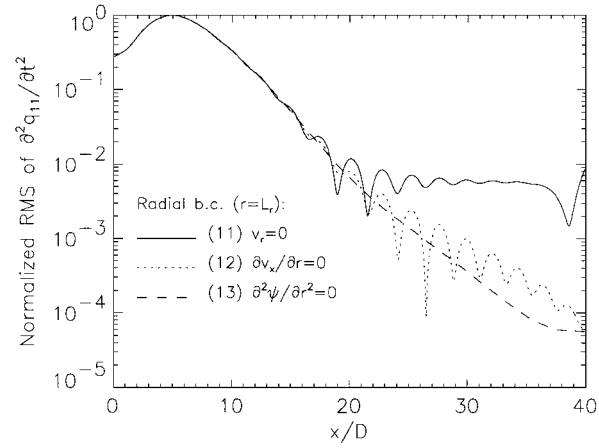

a) Axial quadrupole

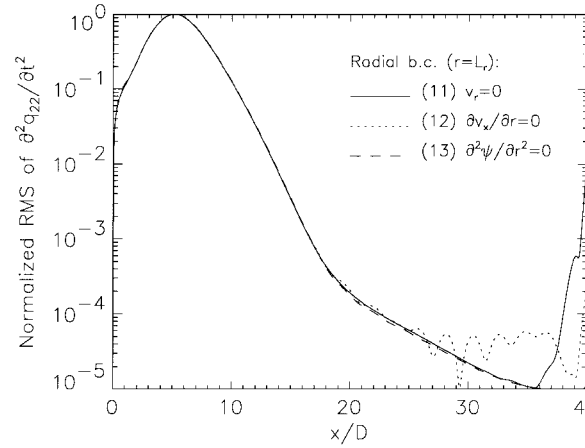

b) Radial quadrupole

Fig. 4 Effect of different radial boundary conditions for ψ on the downstream evolution of the rms of Lighthill's longitudinal quadrupoles per axial length unit given by Eq. (16b); all curves are normalized by the maximum value for the boundary condition (11): $Re_D = 6 \times 10^2$, $R/\delta_2 = 10$, and $L_r = 8R$.

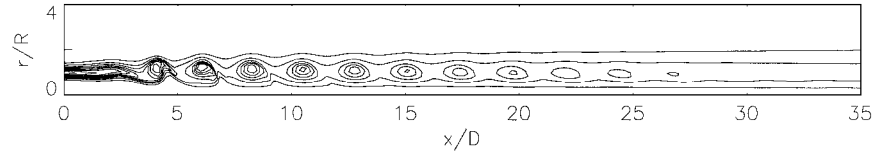

Fig. 3 Instantaneous vorticity contours for the case $Re_D = 1.5 \times 10^3$, $R/\delta_2 = 10$; contour levels are at increments of 0.5 from 0.5 to 6.5.

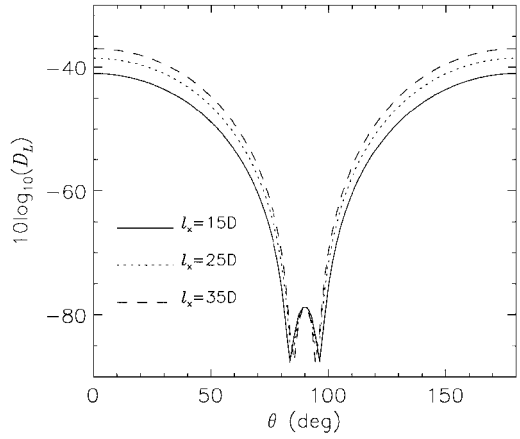

a) $v_r = 0$ by boundary condition (11)

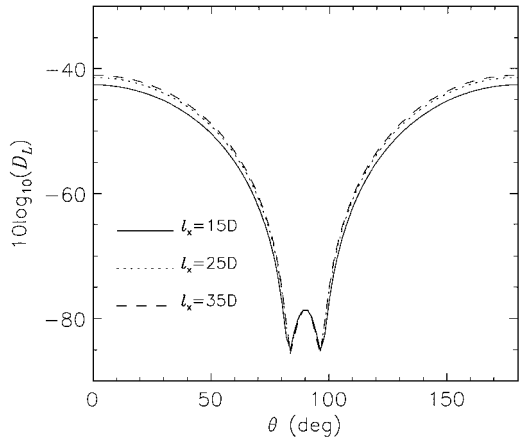

b) $\partial v_x/\partial r = 0$ by boundary condition (12)

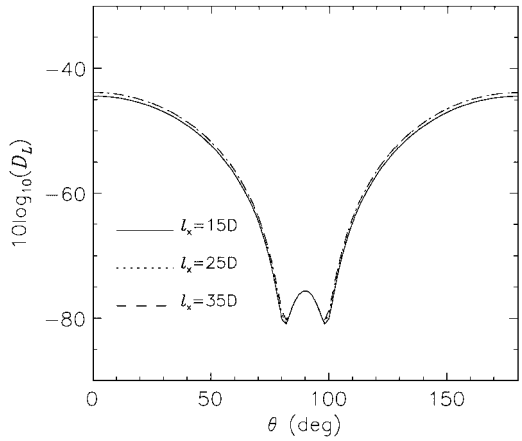

c) $\partial^2\psi/\partial r^2 = 0$ by boundary condition (13)

Fig. 5 Overall directivity by Lighthill's formulation for different acoustic integration lengths l_x and different radial boundary conditions, where $Re_D = 6 \times 10^2$, $R/\delta_2 = 10$, and $L_r = 8R$.

ψ where the constant is determined by the inflow condition for v_x. This constant may contradict the value imposed by the hydrodynamic outflow condition (8). Setting the radial derivative of the axial velocity zero according to boundary condition (12) means that

$$\left.\frac{\partial^2\psi}{\partial r^2}\right|_{r=L_r} = \frac{1}{L_r}\left.\frac{\partial\psi}{\partial r}\right|_{r=L_r} \tag{29}$$

and for $r \gg R$ ψ can be expected to converge to a constant, which means $\partial\psi/\partial r \to 0^+$ by Eq. (6), and hence $\partial^2\psi/\partial r^2 \to 0^-$, which contradicts Eq. (29). Such a contradiction does not exist for boundary condition (13).

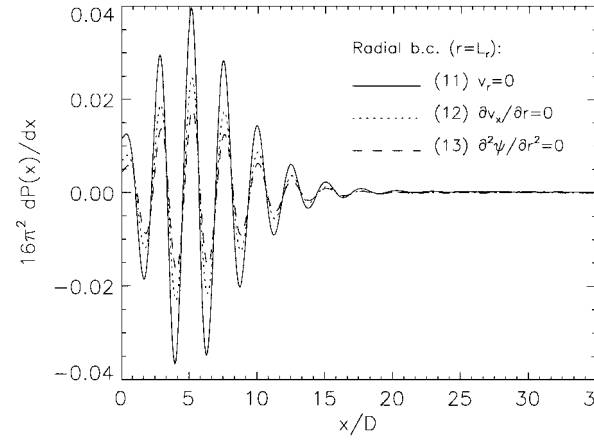

a)

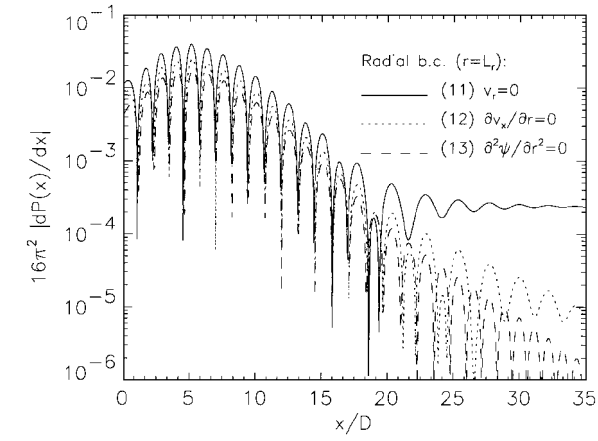

b)

Fig. 6 Axial distribution of the acoustic power output per axial unit length according to Lighthill's formulation (17): $Re_D = 6 \times 10^2$, $R/\delta_2 = 10$, and $L_r = 8R$.

By calculating the main wave number from Fig. 6, it can be shown that U_c is about 70% of U_J, which is in the experimental range found for turbulent jets.[23] Thus, for the following directivity and frequency spectrum, calculations U_c of Eq. (18) were taken as 0.7 U_J. That change only affected the fine details of the acoustic results. In these calculations, l_x was chosen so as to provide a similar damping ratio for the packet amplitude at $x = l_x$ for both cases of Re_D. Radial box lengths, L_r of $8R$ and $6R$ for $Re_D = 6 \times 10^2$ and 1.5×10^3, respectively, were found sufficient, when boundary condition (13) was used.

The directivity plots in Fig. 7a show that increasing Re_D from 6×10^2 to 1.5×10^3 or decreasing δ_2 causes an overall higher sound emission and a convergence toward Möhring's inviscid directivity pattern with two profound minima. This effect agrees with Fig. 2, which showed a corresponding decrease in the axial damping of the mean velocity due to Re_D and in the velocity perturbation due to Re_D and δ_2. This leads to a longer mixing region and, thus, to a higher sound emission.[24] The location of the minimum at $\theta = 65$–70 deg found for $Re_D = 1.5 \times 10^3$ agrees well with the location found by Mitchell et al.[7] for $Re_D = 2.5 \times 10^3$ and $M_J = 0.4$. That means a phase shift of about 160 deg and an amplitude ratio of about 0.4 between $\ddot{Q}_{22}$ and $\ddot{Q}_{11}$, which are close to the theoretical values of 180 deg and 0.5 for the inviscid case by Möhring's theory. However, it should be noted that other effects not taken into account in the present calculations, such as refraction, tend to reduce the axial emission.[25]

The frequency spectrum shown in Fig. 7b has a structure of distinctive peaks as expected from forced jets. The lack of broadband spectra is due to the absence of small scales in the jets. The figure shows a dominance of the shear noise ($St_D = 0.3$) over the self noise ($St_D = 0.6$) as was assumed in the wave packet model of Sec. III.A. The effect of Re_D and δ_2 is the same as in the directivity plots,

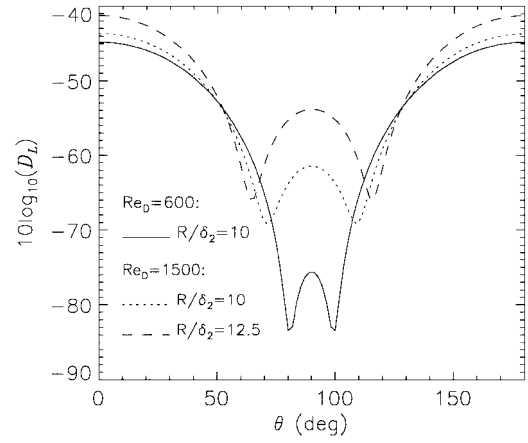

a) Directivity

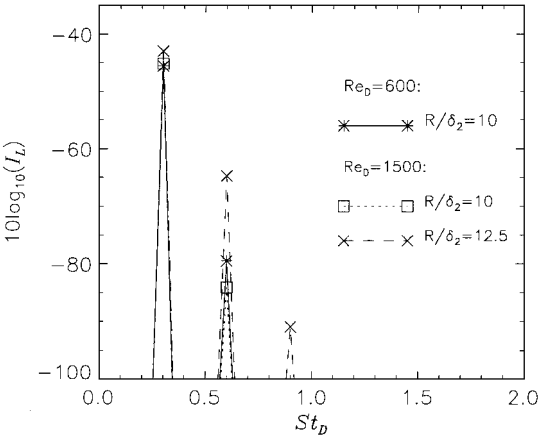

b) Frequency spectrum

Fig. 7 Overall directivity and frequency spectrum by Lighthill's formulation with Eq. (13) as the radial boundary condition, where $l_x = 25D$ for $Re_D = 6 \times 10^2$ and $l_x = 30D$ for $Re_D = 1.5 \times 10^3$.

except for the self noise, which is higher at $Re_D = 6 \times 10^2$ than at 1.5×10^3. This is probably because the inflow disturbance amplitude is in the same order as the maximum perturbation inside the box for $Re_D = 6 \times 10^2$ (Fig. 2), causing a strong finite box size effect in that case. It also shows that the growth in the radial emission as Re_D was increased from 6×10^2 to 1.5×10^3 was mainly due to the shear noise, showing that the effect of the mean radial velocity should not be ignored.

Möhring–Kambe's formulation showed a weaker sensitivity to the DNS radial boundary conditions than Lighthill's formulation due to its use of the vorticity field as the main source. In any case, boundary condition (13) was preferred because of the direct dependence of $\ddot{K}_M$ on the velocity field in Eq. (21d). Figure 8 shows the ratio of the acoustic power output using Möhring–Kambe's formulation to that with Lighthill's for $Re_D = 1.5 \times 10^3$, where a similar behavior was found for $Re_D = 6 \times 10^2$. It can be seen that implementing Eq. (21) without any boundary correction leads to a severe distortion in the calculation. The boundary correction in Eq. (23), which is based on a frozen structure assumption, shows an ability to reduce the dependence on x_a as argued in Sec. III. However, the superiority of the boundary correction in Eq. (24), which was developed to eliminate this dependence, is clear. Its good agreement with the prediction of Lighthill's formulation means that the dominant part of the sound source was captured by the simulation. The difference between using $g_M = 0$ and estimating it by Eq. (28) is relatively small. However, the effect of Eq. (28) on the fine details of the sound emission was found to be sensitive to the value of U_c, and in some cases it actually reduced the agreement with the results from Lighthill's formulation, particularly at $Re_D = 6 \times 10^2$. Therefore, g_M was set to zero in the following results.

Figure 9 shows the directivities and frequency spectra computed using Eq. (24) and $g_M = 0$. Increasing Re_D from 6×10^2 to

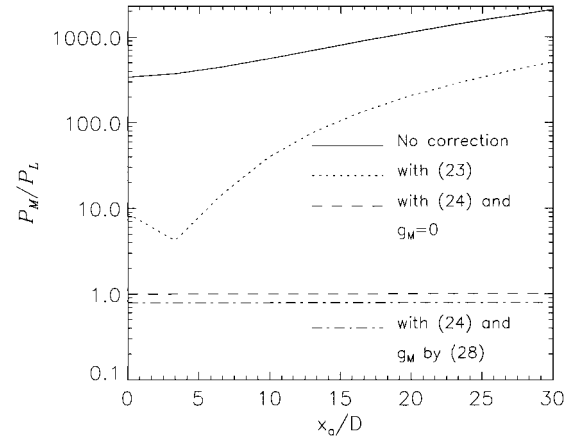

Fig. 8 Effects of streamwise corrections for Möhring–Kambe's formulation on the ratio of its acoustic power output P_M to the acoustic power output by Lighthill's formulation, P_L, where x_a is the axial location of the coordinate origin, $Re_D = 1.5 \times 10^3$, $R/\delta_2 = 10$, and $l_x = 30D$.

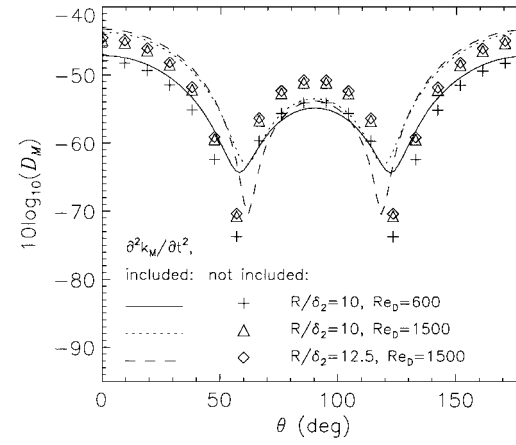

a) Directivity

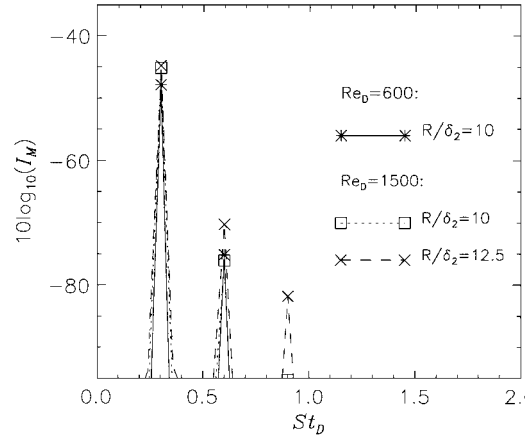

b) Frequency spectrum with $\partial^2 K_M/\partial t^2$ accounted for

Fig. 9 Overall directivity and frequency spectrum using Möhring–Kambe's formulation with Eq. (24) and $g_M = 0$; the rest of the conditions are the same as in Fig. 7.

1.5×10^3 or decreasing δ_2 causes a higher overall sound emission as in Lighthill's formulation. However, there is a marked difference in this effect between the two formulations. That difference is relatively small in the axial emission, only a few decibels, but it becomes significant in the weak radial emission especially for $Re_D = 6 \times 10^2$. Furthermore, one would expect that an increase in Re_D would cause a decrease in the contribution of $\ddot{K}_M$. This is not supported by the results of Fig. 9a, which show, nevertheless, that the overall contribution of $\ddot{K}_M$ is small. Figure 9b shows that Möhring–Kambe's formulation predicts frequency spectra similar

to those of Lighthill's formulation. However, the Möhring–Kambe formulation yields a reduced difference in the shear noise between $R/\delta_2 = 12.5$ and $R/\delta_2 = 10$ at $Re_D = 1.5 \times 10^3$ and similarly in the self noise between $Re_D = 1.5 \times 10^3$ and $Re_D = 6 \times 10^2$.

Other flow configurations were also investigated, such as replacing the inflow condition of zero radial velocity (5) by a zero axial derivative of the radial velocity or adding a second frequency to the inflow disturbance at $St_D = 0.15$. Both configurations showed a similar behavior of the acoustic results to the earlier one. The main change was in the axial emission, with a reduction of a few decibels due to the change in the inflow radial velocity and a smaller increase due to the addition of the second frequency. The latter case showed a wave packet source for each frequency, with about the same U_c and only a weak nonlinear interaction between the two packets, as argued by Crighton and Huerre.[4]

V. Conclusions

The study has dealt with basic radiation calculation for axisymmetric jets. This particular case was chosen because of the ability to deal with a three-dimensional source in the relatively low cost of a two-dimensional simulation. This allowed a comparison of aeroacoustic formulations that were specifically developed for the three-dimensional case. The jet was simulated by an incompressible spatial direct numerical simulation, and the basic radiation was calculated according to Lighthill's and Möhring–Kambe's formulations. It was found that the acoustic results are much more sensitive to numerical constraints, such as the computational box size and boundary conditions, than the hydrodynamic results. This was attributed to the oscillatory behavior of the acoustic source in a form of a wave packet, which results in a much lower level of energy calculated as sound compared to the hydrodynamic energy. Specifically, Lighthill's formulation showed severe sensitivity to the DNS radial boundary condition imposed on the velocity field. Several possible boundary conditions were tested. A zero second-order radial derivative for the stream function was found to be the best, and a zero radial velocity condition was found to be the worst.

The Möhring–Kambe formulation showed a smaller sensitivity to the DNS radial boundary conditions than Lighthill's, but it showed a strong sensitivity to the noncompactness of the hydrodynamic field in the axial direction caused by the finite length of the computational box. A boundary correction developed to remove this sensitivity worked well when the DNS resolution was adequate. It achieved a good agreement with the results from Lighthill's formulation in the total acoustic power output and the emission in the axial direction. However, the agreement was less good for secondary acoustic data, indicating that some effects from the finite computational box still remained. Further reductions in these effects remain an objective for future work, as well as the inclusion of the retarded time variation and the introduction of a time dependence in the radial boundary conditions.

Acknowledgments

This study was supported by British Aerospace, Sowerby Research Centre. The fourth author was supported by the National Research Council of Brazil, Conselho Nacional de Desenvolvimento Cientifico e Tecnologico.

References

[1]Crighton, D. G., "Basic Principles of Aerodynamic Sound Generation," *Progress in Aerospace Sciences*, Vol. 16, No. 1, 1975, pp. 31–96.

[2]Crow, S. C., and Champagne, F. H., "Orderly Structure in Jet Turbulence," *Journal of Fluid Mechanics*, Vol. 48, Aug. 1971, pp. 547–591.

[3]Kibens, V., "Discrete Noise Spectrum Generated by an Acoustically Excited Jet," *AIAA Journal*, Vol. 18, No. 4, 1980, pp. 434–441.

[4]Crighton, D. G., and Huerre, P., "Shear Layer Pressure Fluctuations and Superdirective Acoustic Sources," *Journal of Fluid Mechanics*, Vol. 220, Nov. 1990, pp. 355–368.

[5]Avital, E. J., and Sandham, N. D., "A Note on the Structure of the Acoustic Field Emitted by a Wave Packet," *Journal of Sound and Vibration*, Vol. 204, No. 3, 1997, pp. 533–539.

[6]Avital, E. J., and Sandham, N. D., "Box Length Requirements for Simulation of Sound from Large Structures in Jets," *AIAA Journal*, Vol. 35, No. 5, 1997, pp. 912–915.

[7]Mitchell, B. E., Lele, S. K., and Moin, P., "Direct Computation of the Sound Generated by Vortex Pairing in an Axisymmetric Jet," AIAA Paper 95-0504, Jan. 1995.

[8]Crighton, D. G., "Computational Aeroacoustics for Low Mach Number Flows," *Computational Aeroacoustics*, edited by J. C. Hardin and M. Y. Hussaini, Springer–Verlag, New York, 1993, pp. 50–68.

[9]Wang, M., Lele, S. K., and Moin, P., "Sound Radiation During Local Laminar Breakdown in a Low-Mach-Number Boundary Layer," *Journal of Fluid Mechanics*, Vol. 319, July 1996, pp. 197–218.

[10]Wang, M., Lele, S. K., and Moin, P., "Computation of Quadrupole Noise Using Acoustic Analogy," *AIAA Journal*, Vol. 34, No. 11, 1996, pp. 2247–2254.

[11]Avital, E. J., Sandham, N. D., and Luo, K. H., "Mach Wave Radiation by Mixing Layers. Part I: Analysis of the Sound Field," *Theoretical and Computational Fluid Dynamics*, Vol. 12, No. 2, 1998, pp. 73–90.

[12]Musafir, R. E., "On the Sound Field of Organized Vorticity in Jet Flows," *Proceedings of the 13th International Congress on Acoustics*, edited by P. Pravica and G. Drakulic, Vol. 2, SAVA CENTAR, Belgrade, Yugoslavia, 1989, pp. 63–66.

[13]Bridges, J. E., and Hussain, A. K. M. F., "Roles of Initial Condition and Vortex Pairing in Jet Noise," *Journal of Sound and Vibration*, Vol. 117, No. 2, 1987, pp. 289–311.

[14]Sandham, N. D., and Reynolds, W. C., "A Numerical Investigation of the Compressible Mixing Layer," Thermosciences Div., Rept. TF-45, Dept. of Mechanical Engineering, Stanford Univ., Stanford, CA, Sept. 1989.

[15]Grinstein, F. F., and Devore, C. R., "Dynamics of Coherent Structures and Transition to Turbulence in Free Square Jets," *Physics of Fluids*, Vol. 8, No. 5, 1996, pp. 1237–1251.

[16]Michalke, A., "Survey on Jet Instability Theory," *Progress in Aerospace Sciences*, Vol. 21, No. 3, 1984, pp. 159–199.

[17]Gresho, P. M., "Some Current CFD Issues Relevant to the Incompressible Navier–Stokes Equations," *Computer Methods in Applied Mechanics and Engineering*, Vol. 87, No. 2-3, 1991, pp. 201–251.

[18]Lighthill, M. J., "A General Introduction to Aeroacoustics and Atmospheric Sound," *Computational Aeroacoustics*, edited by J. C. Hardin and M. Y. Hussaini, Springer–Verlag, New York, 1993, pp. 3–40.

[19]Peyret, R., and Taylor, T. D., *Computational Methods for Fluid Flow*, Springer–Verlag, New York, 1983, pp. 141–207.

[20]Kambe, T., "Influence of Viscosity on the Aerodynamic Sound Emission in a Free Space," *Journal of Sound and Vibration*, Vol. 95, No. 3, 1984, pp. 351–360.

[21]Lighthill, M. J., "On Sound Generated Aerodynamically II. Turbulence as a Source of Sound," *Proceedings of the Royal Society of London*, Vol. A222, Feb. 1954, pp. 1–32.

[22]Huerre, D., and Crighton, D. G., "Sound Generation by Instability Waves in a Low Mach Number Jet," AIAA Paper 83-0661, April 1983.

[23]Bradshaw, P., Ferriss, D. H., and Johnson, R. F., "Turbulence in the Noise-Producing Region of a Circular Jet," *Journal of Fluid Mechanics*, Vol. 19, Aug. 1964, pp. 591–624.

[24]Lilley, G. M., "On the Noise from Air Jets," Aeronautical Research Council 20376, College of Aeronautics, Cranfield, England, UK, Sept. 1958.

[25]Ribner, H. S., "Effects of Jet Flow on Jet Noise via an Extension to the Lighthill Model," *Journal of Fluid Mechanics*, Vol. 321, Aug. 1996, pp. 1–24.

P. Givi
Associate Editor